ARTICLE IN PRESS

Nature Communications

https://doi.org/10.1038/s41467-026-68935-x

Article in Press

Growth of rhombohedral-stacked single-crystal WS_2/MoS_2 vertical heterostructures

Received: 12 September 2025

Accepted: 21 January 2026

Cite this article as: Chen, J., Guo, Y., Zhang, Y. *et al.* Growth of rhombohedral-stacked single-crystal WS_2/MoS_2 vertical heterostructures. *Nat Commun* (2026). https://doi.org/10.1038/s41467-026-68935-x

Junting Chen, Yanqing Guo, Yixu Zhang, Zelin Li, Quanlin Guo, Qiu Yang, Kuan Li, Yongqing Zhang, Baoying Zhang, Yi Hu, Yingying Cai, Zhen Hu, Qingqiu Cheng, Xinpeng Liu, Meizhuang Liu, Jiewei Chen, Qinghong Yuan, Kaihui Liu & Xiaozhi Xu

We are providing an unedited version of this manuscript to give early access to its findings. Before final publication, the manuscript will undergo further editing. Please note there may be errors present which affect the content, and all legal disclaimers apply.

If this paper is publishing under a Transparent Peer Review model then Peer Review reports will publish with the final article.

ARTICLE IN PRESS

© The Author(s) 2026. **Open Access** This article is licensed under a Creative Commons Attribution-NonCommercial-NoDerivatives 4.0 International License, which permits any non-commercial use, sharing, distribution and reproduction in any medium or format, as long as you give appropriate credit to the original author(s) and the source, provide a link to the Creative Commons licence, and indicate if you modified the licensed material. You do not have permission under this licence to share adapted material derived from this article or parts of it. The images or other third party material in this article are included in the article's Creative Commons licence, unless indicated otherwise in a credit line to the material. If material is not included in the article's Creative Commons licence and your intended use is not permitted by statutory regulation or exceeds the permitted use, you will need to obtain permission directly from the copyright holder. To view a copy of this licence, visit http://creativecommons.org/licenses/by-nc-nd/4.0/.

Growth of rhombohedral-stacked single-crystal WS_2/MoS_2 vertical heterostructures

Junting Chen[1,2#], Yanqing Guo[3#], Yixu Zhang[1,2], Zelin Li[4], Quanlin Guo[5], Qiu Yang[5], Kuan Li[1,2], Yongqing Zhang[1,2], Baoying Zhang[1,2], Yi Hu[1,2], Yingying Cai[1,2], Zhen Hu[1,2], Qingqiu Cheng[1,2], Xinpeng Liu[1,2], Meizhuang Liu[1,2], Jiewei Chen[4], Qinghong Yuan[3]*, Kaihui Liu[5,6]*, and Xiaozhi Xu[1,2]*

[1] Guangdong Basic Research Center of Excellence for Structure and Fundamental Interactions of Matter, Guangdong Provincial Key Laboratory of Quantum Engineering and Quantum Materials, School of Physics, South China Normal University, Guangzhou 510006, China

[2] Guangdong-Hong Kong Joint Laboratory of Quantum Matter, Frontier Research Institute for Physics, South China Normal University, Guangzhou 510006, China

[3] State Key Laboratory of Precision Spectroscopy, School of Physics and Electronic Science, East China Normal University, 500 Dongchuan Road, Minhang, Shanghai 200241, China

[4] Flexible Photonic Chip International Innovation Centerof Guangdong-Hong Kong-Macao Greater Bay Area, School of Optoelectronic Science and Engineering, South China Normal University, Guangzhou 510631, China

[5] State Key Laboratory for Mesoscopic Physics, Frontiers Science Center for Nano-optoelectronics, School of Physics, Peking University, Beijing 100871, China

[6] Songshan Lake Materials Laboratory, Institute of Physics, Chinese Academy of Sciences, Dongguan 523808, China

# These authors contributed equally to this work

* Correspondence: xiaozhixu@scnu.edu.cn; qhyuan@phy.ecnu.edu.cn; khliu@pku.edu.cn

Abstract

Vertical van der Waals heterostructures (vdWHs), formed through layer-by-layer stacking of two-dimensional materials, offer appealing opportunities for exploring novel physics and potential applications. However, the conventional approach of mechanical exfoliation followed by manual stacking faces significant challenges in achieving atomically clean interfaces and large size, severely limiting practical applications. Here, we proposed a comprehensive mechanism governing nucleation, orientation and stack control of vertical vdWHs during chemical vapour deposition (CVD) and demonstrated the layer-by-layer epitaxial growth of 1 cm × 1 cm sized single-crystal, rhombohedral-stacked WS_2/MoS_2 films. First-principles calculations reveal that sulphur (S) vacancies in the underlying MoS_2 layer preferentially form at step edges. These S vacancies serve as nucleation sites for the upper WS_2 layer and enhance symmetry breaking between rhombohedral- and hexagonal-stacked WS_2/MoS_2. Leveraging this mechanism, we achieved unidirectionally aligned WS_2 islands on MoS_2 substrate that seamlessly coalesce into continuous single-crystal WS_2/MoS_2 films. Systematic characterizations confirmed the single-crystal nature and rhombohedral-stacked configuration, while revealing the ferroelectric properties and self-driven photoelectric response in the resulting heterostructures. Our work establishes a fundamental mechanism for controlled growth of single-crystal vertical heterostructures, providing a robust foundation for scalable manufacturing and future industrial applications.

Introduction

Vertical van der Waals heterostructures (vdWHs), which are constructed by sequentially stacking two-dimensional (2D) materials, have emerged as a transformative platform for exploring exotic physics and facilitating the development of next-generation electronic devices[1-3]. In contrast to conventional semiconductor heterostructures that are limited by lattice matching and chemical compatibility constraints, 2D materials offer unprecedented flexibility due to their in-plane covalently bonded lattices and weak out-of-plane van der Waals interactions. This unique combination has enabled researchers to artificially engineer novel vertical heterostructures with tailored properties, unveiling remarkable phenomena such as moiré excitons[4,5], moiré superlattices[6-8], and emergent ferroelectricity[9-11].

However, realizing the full potential of vdWHs faces a fundamental manufacturing challenge. The prevailing method, which involves mechanical exfoliation followed by manual stacking, suffers from inherent limitations: contaminated interfaces, poor reproducibility, and restricted lateral dimensions at the microscopic level[12,13]. These constraints severely hinder scalable production and practical applications. Consequently, the direct chemical vapour deposition (CVD) growth of large-area, high-quality vertical vdWHs, particularly single crystals, has become a critical technological imperative.

Among the various CVD strategies, layer-by-layer epitaxial growth provides distinct advantages over one-step synthesis by enabling superior nucleation control and facilitating large-area uniformity[14-22]. Nevertheless, a fundamental crystallographic challenge persists for transition metal dichalcogenide heterostructures (TMDHs). Owing to their non-centrosymmetric crystal structure, the upper layer inevitably exhibits two energetically equivalent but antiparallel orientations during growth, resulting in a mixture of rhombohedral and hexagonal stacking configurations within the same sample[23,24]. This orientation degeneracy prevents the formation of single-crystal vertical TMDHs, a prerequisite for many applications requiring uniform electronic properties.

Previous advancements in growing single-crystal 2D materials, such as hexagonal boron nitride (hBN) and TMDs, have shown that atomic steps on the substrate can break the orientation degeneracy and promote unidirectional alignment[25-29]. However, applying this approach to the growth of vertical TMDHs presents unique complications: the upper layer grows on a substrate already covered by the lower TMD layer, making the conventional step-guided growth mechanism ineffective. A critical question thus arises: how can we achieve precise nucleation site control and orientation selectivity in this more complex growth system?

Here, we addressed this challenge by proposing and experimentally demonstrating a mechanism for the controlled growth of single-crystal bilayer vertical TMDHs. Through first-principles calculations, we revealed that sulfur (S) vacancies, defects commonly present in CVD-grown MoS_2, tend to form preferentially at step edges and serve dual roles: (1) acting as preferred nucleation sites for the upper WS_2 layer, and (2) breaking the energetic degeneracy between rhombohedral and hexagonal stacking configurations. Guided by this mechanism, we successfully realized the epitaxial growth of unidirectionally aligned WS_2 islands on MoS_2 substrates and 1 cm × 1 cm sized single-crystal WS_2/MoS_2 films. Our work establishes a comprehensive framework for orientation-controlled growth of single-crystal vertical heterostructures, opening pathways for scalable production of high-quality 2D devices and enabling a systematic exploration of their unique properties.

Results

Different growth behaviours of WS_2 on MoS_2/sapphire substrates

In the layer-by-layer growth of WS_2/MoS_2 heterostructures, achieving unidirectional alignment of the upper WS_2 islands is a crucial prerequisite for constructing high-quality heterostructures. To this end, we systematically investigated the growth behaviour of WS_2 on MoS_2 under various conditions using first-principles calculations, with an emphasis on the underlying mechanisms by which substrate structure and defects influence the orientation of WS_2 islands.

We first examined the growth behaviour of WS_2 when using MoS_2 films grown on ideal c-plane sapphire surfaces as templates (Fig. 1a). By calculating the binding energy between WS_2 islands and the underlying MoS_2 at different rotation angles (θ = 0°-60°, with 10° intervals), we found that two configurations, θ = 0° (rhombohedral stacking) and θ = 60° (hexagonal stacking), exhibit the lowest energies. However, the energy difference between these two orientations is only 0.12 eV/nm² (Fig. 1b), indicating that under thermodynamic equilibrium conditions, the occurrence probabilities of both orientations are essentially equal, thus making unidirectional alignment impossible. This result is consistent with expectations: given that both WS_2 and MoS_2 possess three-fold symmetry, the upper WS_2 naturally exhibits two antiparallel preferred orientations. This theoretical prediction is highly consistent with our experimental observations: vertical vdWHs always exhibit islands with two antiparallel orientations simultaneously during growth (Fig. 1c).

Based on previous studies showing that stepped substrates can improve orientation control of TMDs[26,29], we further investigated the WS_2 growth behaviour when using MoS_2 films grown on stepped sapphire surfaces as templates (Fig. 1d). We focused on analysing the relative stability of WS_2 islands with different orientations near step edges (Fig. 1e). The calculation results show that while the introduction of steps indeed makes the rhombohedral stacking configuration more stable, the energy difference between the two configurations only increases to 0.31 eV/nm². In this scenario where the step edge is merely strained but free of defects, this minor energy difference confirms that interfacial strain alone is not a sufficient driving force for selective growth under typical experimental conditions. And experimental results also confirm that WS_2 islands still exhibit bidirectional distribution (Fig. 1f).

Given that S vacancies are commonly observed in MoS_2 under typical CVD growth conditions, we investigated their role in directing WS_2 growth[30-33]. This focus is further justified by density functional theory (DFT) calculations, which confirm that the formation energy of a molybdenum (Mo) vacancy (8.19 eV) is significantly higher than that of an S vacancy (3.65 eV). This suggests that S vacancies are the dominant point defect. Consequently, we systematically studied the effect of S vacancies on the growth orientation of WS_2. When S vacancies are introduced in MoS_2 near step edges (Fig. 1g), the energy difference between $\theta = 0°$ and $\theta = 60°$ structures significantly increases to 0.84 eV/nm² (Fig. 1h). This symmetry breaking is driven by a powerful and highly specific edge-binding mechanism at the atomic scale. The S vacancies create reactive Mo sites at the step edge, which can form strong chemical bonds exclusively with the edge of a 0°-oriented WS_2 cluster, thus providing this substantial energetic advantage. This substantial increase in energy difference has important practical significance. To further verify the robustness of this vacancy-driven mechanism, we systematically calculated the energy difference across a wide range of S vacancy concentrations, from 17% to 88%. Remarkably, our results show that the energetic preference for the 0° orientation is exceptionally stable, with the energy difference remaining consistently large, fluctuating only slightly between 0.77 and 0.88 eV/nm² (see Supplementary Fig. 1). Based on Boltzmann distribution calculations, at a growth temperature of 1000°C, the nucleation probability of rhombohedral stacking is significantly higher than that of hexagonal stacking. This theoretical prediction, which holds true across a broad process window, aligns closely with the unidirectional alignment phenomenon observed in experiments (Fig. 1i and Supplementary Fig. 2), indicating that S vacancies play a critical role in achieving WS_2 orientation control. Crucially, our analysis shows that this mechanism does not depend on a specific critical or optimal vacancy concentration. The energetic preference for the 0° orientation is established as long as vacancies are present to create reactive binding sites, making the process highly robust and reproducible across a wide range of experimental conditions where S vacancies are thermodynamically favourable.

Selective formation of S vacancies near step edges

Although we have demonstrated that introducing S vacancies are likely to facilitate the preparation of unidirectionally aligned WS_2/MoS_2 samples, it is critical to ensure that these vacancies predominantly form at the step edges rather than on the terraces. To verify this hypothesis, we first analysed the stress distribution in stepped MoS_2 structures (Fig. 2a). The calculation results clearly show that S atoms below the step edges experience the maximum stress (deepest red regions in Fig. 2a), with an average bond length stretching of 1.4%, indicating significant stress concentration effects in this region. Based on these stress analysis results, we systematically evaluated the formation energies of S vacancies at different positions near MoS_2 steps (Fig. 2b-c). Our findings reveal that the formation energy of S vacancies at step edges (position S_5) is substantially lower than that on the terrace (position S_8) by approximately 0.84 eV. This significant energy difference arises from the varying degrees of stress release when defects form at different positions: the high-stress environment at step edges makes vacancy formation thermodynamically more favourable.

Further thermodynamic analysis reveals that on MoS_2 with S vacancies at step edges, the Gibbs free energy of WS_2 islands decreases by 0.35 eV and 0.17 eV compared to the terrace and vacancy-free step edges, respectively (Fig. 2d). This significant energy advantage ensures the preferential nucleation of WS_2 at step edges, thereby providing critical spatial selectivity for achieving orientation and stack control. Through differential charge density analysis, we further revealed the microscopic mechanism underlying the promotion of unidirectional alignment by S vacancies: compared to ideal MoS_2 at the terrace or steps, MoS_2 with S vacancies at step edges undergo significant charge transfer (Fig. 2e-g). This charge redistribution facilitates stronger bonding interactions between WS_2 and the underlying MoS_2, thus energetically favouring unidirectional growth.

Growth of single-crystal WS_2/MoS_2 films

Guided by this mechanism, we successfully achieved the production of 1 cm × 1 cm sized single-crystal WS_2/MoS_2 films by replacing the lower-layer MoS_2 islands with single-crystal MoS_2 films (Fig. 3a and Supplementary Fig. 3-5). Firstly, single-crystal MoS_2 films were produced on sapphire substrates by seamless stitching of unidirectionally aligned islands (Fig. 3b-c). Before the subsequent growth of upper-layer WS_2, the MoS_2 samples were first annealed at 500°C for 30 min in a vacuum environment to selectively produce S vacancies in the lower-layer MoS_2 sample (the direct characterizations of S vacancies are shown in Supplementary Fig. 6-7)[34]. Finally, the tungsten source was introduced to the CVD system to finalize the growth of WS_2/MoS_2 samples (Fig. 3a). In accordance with theoretical expectations, we observed preferential nucleation of unidirectionally aligned WS_2 at step edges with short growth time and continuous WS_2/MoS_2 films after long time growth (Fig. 3d-e and Supplementary Fig. 8). To validate the universality of our mechanism, we also grew WS_2 islands on WSe_2 samples. The unidirectionally aligned WS_2 obtained on WSe_2 clearly demonstrated that this mechanism could also be applied to other TMD heterostructures (Supplementary Fig. 9).

Characterizations of single-crystal WS_2/MoS_2 films

To check the quality and stacking configurations of the as-grown WS_2/MoS_2 samples, systematic characterization techniques were conducted, and the results undoubtedly proved the high quality, single-crystal nature and rhombohedral-stacked structure. Photoluminescence (PL) and Raman spectroscopy were first carried out to characterize the composition and uniformity. The simultaneous appeared PL and Raman peaks corresponding to WS_2 and MoS_2 demonstrated the formation of vertical WS_2/MoS_2 heterostructure (Fig.4a-b). Then the line scan Raman mapping over a range of 1 centimetre, Raman and PL mapping with $100 \times 100\ \mu m^2$ size at different positions revealed its high uniformity (Fig.4c-d and Supplementary Fig. 10). Subsequently, atomic-resolved atomic force microscopy (AFM) was employed to confirm the uniformity of the sample and the seamless stitching of two connected WS_2 islands on MoS_2 (Supplementary Fig. 11-12). The perfect lattice structure at merged areas demonstrated that no boundary was formed (Supplementary Fig. 12). Also, various atomic AFM images and the polarized second-harmonic generation (SHG) patterns acquired over different positions further confirmed the unidirectional alignment at large scale (Fig. 4e-f and Supplementary Fig. 13-14).

Then, the stacking configuration of the WS_2/MoS_2 samples was verified through microscopic aberration-corrected transmission electron microscopy (TEM) and macroscopic SHG measurements. The atomically-resolved cross-section TEM image first provide the most direct evidence for the rhombohedral lattice (Fig. 4g). Due to the distinct symmetries of the rhombohedral- and hexagonal-stacked WS_2/MoS_2 samples, the SHG intensity of these two configurations are quite different. The SHG intensity of rhombohedral-stacked heterostructure is obviously enhanced, while hexagonal-stacked heterostructure exhibited negligible SHG signals[9]. The obtained SHG mapping of WS_2 islands on MoS_2 sample further demonstrated the rhombohedral structure (Supplementary Fig. 15), and the uniform SHG mapping at different positons proved the identical stack of the WS_2/MoS_2 film at large scale (Supplementary Fig. 16). It has been reported that a unique ferroelectricity can be found in untwisted commensurate MoS_2/WS_2 samples[9], and this property was also observed in our sample both by piezoelectric force microscope (PFM) and electrical measurements (Fig. 4h and Supplementary Fig. 17). We further checked the quality of our samples by fabricating devices using both monolayer WS_2 samples and WS_2/MoS_2 heterostructures. Our results indicate that the WS_2/MoS_2 heterostructure exhibits significantly superior performance in terms of carrier mobility and self-driven photoelectric response (Supplementary Fig. 18).

Discussion

In summary, we proposed an S vacancy/step-guided epitaxy mechanism for the growth of rhombohedral-stacked single-crystal WS_2/MoS_2 films. We revealed that the presence of S vacancies can address the issue of nucleation position, lattice orientation and the stacking configurations, which are all critical factors in the final production of WS_2/MoS_2 single crystals. With this mechanism, 1 cm × 1 cm sized rhombohedral-stacked single-crystal WS_2/MoS_2 films has been successfully produced.

Methods

Growth of single-crystal MoS_2 monolayer on c-plane sapphire. MoS_2 monolayer islands and films were grown on *c*-plane sapphire in a CVD system with three temperature zones, namely, zones I–III. Sulfur (600 mg, Alfa Aesar, 99.5%) powder was placed at the upstream end of a quartz tube and heated by a heating belt. The precursor solutions with a concentration of 18 mg/ml was prepared by dissolving $Na_2MoO_4 \cdot 2H_2O$ (Alfa Aesar, 98%) in deionized water, which was sprayed on the sapphire substrate. The sapphire substrate supported by a quartz plate was vertically positioned above another sapphire substrate spray-coated with a sodium molybdate solution, forming an enclosed space. The sapphire substrates were placed in zone II. During the growth process, the temperature zone II and III of the tube furnace were heated to 950 ℃ within 40 min. The S source started to heat at 28 min and the temperature up to 160 ℃ within 15 min. Ar gas flow (25 sccm) was maintained during the whole process. At 35 min, an additional oxygen flow of 1.2 sccm was introduced. At 60 min, the oxygen flow rate was discontinued. The growth time was 20-40 min to obtain MoS_2 islands or films and the whole CVD system was cooled down naturally to room temperature after growth.

Growth of single-crystal WS_2/MoS_2 on c-plane sapphire. WS_2 monolayer islands and films were grown on *c*-plane sapphire substrate pre-coated with MoS_2 films in a CVD system with three temperature zones, namely, zones I–III. Sulfur (360 mg, Alfa Aesar, 99.5%) powder was placed at the upstream end of a quartz tube and heated by a heating belt. $WO_{2.9}$ (260 mg, Alfa Aesar, 99.99%) powder and NaCl (26 mg, Alfa Aesar, 99.99%) mixture were placed in zone I of the tube furnace and sapphire substrates were placed in zone II and III. Before the heating process, pumping to vacuum (<10 Pa) to remove any residual H_2O and O_2 in the quartz tube. During the growth process, the temperature zone I of the tube furnace was heated to 520 ℃ within 15 min after a 20-min delay, and then held at 520 ℃ for 15 min. The temperature zone II and III of the tube furnace were heated to 1030 ℃ within 40 min. The S source started to heat at 23 min and the temperature up to 135 ℃ within 12 min. Ar gas flow (15 sccm) was maintained during the whole process. The growth time was 10-20 min to obtain WS_2 islands on MoS_2 film or single-crystal WS_2/MoS_2 film and the whole CVD system was cooled down naturally to room temperature after growth.

Characterization.

(i) AFM and PFM measurements were performed using Asylum Cypher S under an atmospheric environment.

(ii) Optical measurements. Optical images were conducted with an Mshot MSX10 microscope. Raman and PL spectra were conducted on a WITec-Alpha300 Raman system with a laser excitation wavelength of 532 nm and power of ~2 mW. SHG mapping was obtained using the same system under excitation from a femtosecond laser centred at 1064 nm with an average power of 300 mW (Rainbow 1064 OEM with pulse duration of 15 ps and repetition rate of 50 MHz).

(iii) TEM measurements were performed in FEI Titan Themis G2 300 operated at 300 kV.

Computational details.

All geometric optimizations and energy calculations in this study were performed using density functional theory (DFT) as implemented in the Vienna Ab initio Simulation Package (VASP). The exchange-correlation interactions were described by the Perdew-Burke-Ernzerhof (PBE) functional within the generalized gradient approximation (GGA). Electron-ion interactions were treated using the projector augmented-wave (PAW) method with a plane-wave basis set employing a cutoff energy of 420 eV. To accurately account for the long-range van der Waals (vdW) interactions essential in layered two-dimensional material systems, we incorporated the DFT-D3 dispersion correction scheme. Atomic structures were relaxed until the energy difference between consecutive steps was less than 10^{-5} eV. Brillouin zone sampling was performed using a 2×1×1 Monkhorst-Pack k-point mesh cantered at the Γ point.

The binding energy (E_b) of a WS_2 nucleus on a MoS_2 surface terrace was calculated as:

$$E_b = (E_{tot} - E_{far})/A \tag{1}$$

where E_{tot} represents the total energy of the composite system with the WS_2 cluster interacting with the MoS_2 surface, E_{far} denotes the total energy of the system with the WS_2 cluster positioned sufficiently far from the MoS_2 plane to eliminate vdW interactions, and A is the area of the WS_2 cluster.

The formation energy ($E_f(V)$) of a S vacancy was determined using:

$$E_f(V) = E_{V\text{-}S} - E_{tot} + \mu_S \tag{2}$$

where $E_{V\text{-}S}$ represents the total energy of the system containing a S vacancy, E_{tot} is the total energy of the pristine MoS_2 without any vacancy, and μ_S is the chemical potential of S, taken as half the energy of an isolated S_2 molecule.

The Gibbs free energy (ΔG) of the WS_2 cluster formation was calculated as:

$$\Delta G = E_f + E_b \tag{3}$$

where $E_f = E_{tot} - n_S \times \mu_S - n_W \times \mu_W$ represents the formation energy of the WS_2 cluster. In this equation, Etot is the total energy of the isolated WS_2 cluster, while n_S and n_W are the numbers of S and W atoms in the cluster, respectively. The terms μ_S and μ_W denote the chemical potentials of S and W atoms, respectively, which were corrected for growth temperature and pressure conditions, yielding values of -4.01 eV for S and -13.64 eV for W. The binding energy (E_b) represents the interaction energy between the WS_2 cluster and the MoS_2 substrate, calculated for different surface configurations including flat terraces, step edges, and S vacancy sites at steps.

Data availability

The Source Data underlying the figures of this study are available with the paper. All raw data generated during the current study are available from the corresponding authors upon request.

References:

1 Geim, A. K. & Grigorieva, I. V. Van der Waals heterostructures. *Nature* **499**, 419-425 (2013).

2 Liu, Y., Weiss, N. O., Duan, X. D., Cheng, H. C., Huang, Y. *et al.* Van der Waals heterostructures and devices. *Nat Rev Mater* **1**, 16042 (2016).

3 Novoselov, K. S., Mishchenko, A., Carvalho, A. & Neto, A. H. C. 2D materials and van der Waals heterostructures. *Science* **353**, aac9439 (2016).

4 Jin, C. H., Regan, E. C., Yan, A. M., Utama, M. I. B., Wang, D. Q. *et al.* Observation of moire excitons in WSe_2/WS_2 heterostructure superlattices. *Nature* **567**, 76-80 (2019).

5 Tran, K., Moody, G., Wu, F. C., Lu, X. B., Choi, J. *et al.* Evidence for moire excitons in van der Waals heterostructures. *Nature* **567**, 71-75 (2019).

6 Regan, E. C., Wang, D. Q., Jin, C. H., Utama, M. I., Gao, B. N. *et al.* Mott and generalized Wigner crystal states in WSe_2/WS_2 moire superlattices. *Nature* **579**, 359-363 (2020).

7 Xu, Y., Liu, S., Rhodes, D. A., Watanabe, K., Taniguchi, T. *et al.* Correlated insulating states at fractional fillings of moire superlattices. *Nature* **587**, 214-218 (2020).

8 McGilly, L. J., Kerelsky, A., Finney, N. R., Shapovalov, K., Shih, E. M. *et al.* Visualization of moire superlattices. *Nat Nanotechnol* **15**, 580-584 (2020).

9 Rogée, L., Wang, L., Zhang, Y., Cai, S. H., Wang, P. *et al.* Ferroelectricity in untwisted heterobilayers of transition metal dichalcogenides. *Science* **376**, 973-978 (2022).

10 Wang, X. R., Yasuda, K., Zhang, Y., Liu, S., Watanabe, K. *et al.* Interfacial ferroelectricity in rhombohedral-stacked bilayer transition metal dichalcogenides. *Nat Nanotechnol* **17**, 367-371 (2022).

11 Weston, A., Castanon, E. G., Enaldiev, V., Ferreira, F., Bhattacharjee, S. *et al.* Interfacial ferroelectricity in marginally twisted 2D semiconductors. *Nat Nanotechnol* **17**, 390-395 (2022).

12 Haigh, S. J., Gholinia, A., Jalil, R., Romani, S., Britnell, L. *et al.* Cross-sectional imaging of individual layers and buried interfaces of graphene-based heterostructures and superlattices. *Nat Mater* **11**, 764-767 (2012).

13 Castellanos-Gomez, A., Duan, X. F., Fei, Z., Gutierrez, H. R., Huang, Y. *et al.* Van der Waals heterostructures. *Nat Rev Method Prime* **2**, 58 (2022).

14 Gong, Y. J., Lin, J. H., Wang, X. L., Shi, G., Lei, S. D. *et al.* Vertical and in-plane heterostructures from WS_2/MoS_2 monolayers. *Nat Mater* **13**, 1135-1142 (2014).

15 Kang, K., Lee, K. H., Han, Y. M., Gao, H., Xie, S. E. *et al.* Layer-by-layer assembly of two-dimensional materials into wafer-scale heterostructures. *Nature* **550**, 229-233 (2017).

16 Li, J., Yang, X. D., Liu, Y., Huang, B. L., Wu, R. X. *et al.* General synthesis of two-dimensional van der Waals heterostructure arrays. *Nature* **579**, 368-374 (2020).

17 Zhou, Z. J., Hou, F. C., Huang, X. L., Wang, G., Fu, Z. H. *et al.* Stack growth of wafer-scale van der Waals superconductor heterostructures. *Nature* **621**, 499-505 (2023).

18 Li, J., Yang, X. D., Zhang, Z. W., Yang, W. Y., Duan, X. D. *et al.* Towards the scalable synthesis of two-dimensional heterostructures and superlattices beyond exfoliation and restacking. *Nat Mater* **23**, 1326-1338 (2024).

19 Gong, Y. J., Lei, S. D., Ye, G. L., Li, B., He, Y. M. *et al.* Two-Step Growth of Two-Dimensional $WSe_2/MoSe_2$ Heterostructures. *Nano Lett* **15**, 6135-6141 (2015).

20 Yang, T. F., Zheng, B. Y., Wang, Z., Xu, T., Pan, C. *et al.* Van der Waals epitaxial growth and optoelectronics of large-scale WSe_2/SnS_2 vertical bilayer p-n junctions. *Nat Commun* **8**, 1906 (2017).

21 Kezilebieke, S., Huda, N., Vano, V., Aapro, M., Ganguli, S. C. *et al*. Topological superconductivity in a van der Waals heterostructure. *Nature* **588**, 424-428 (2020).

22 Jin, G., Lee, C. S., Okello, O. F. N., Lee, S. H., Park, M. Y. *et al.* Heteroepitaxial van der Waals semiconductor superlattices. *Nat Nanotechnol* **16**, 1092-1098 (2021).

23 Zhang, J., Wang, J. H., Chen, P., Sun, Y., Wu, S. *et al.* Observation of Strong Interlayer Coupling in MoS_2/WS_2 Heterostructures. *Adv Mater* **28**, 1950-1956 (2016).

24 Zhang, Q., Xiao, X., Zhao, R. Q., Lv, D. H., Xu, G. C. *et al.* Two-Dimensional Layered Heterostructures Synthesized from Core-Shell Nanowires. *Angew Chem Int Edit* **54**, 8957-8960 (2015).

25 Chen, T. A., Chuu, C. P., Tseng, C. C., Wen, C. K., Wong, H. S. P. *et al.* Wafer-scale single-crystal hexagonal boron nitride monolayers on Cu (111). *Nature* **579**, 219-223 (2020).

26 Li, T. T., Guo, W., Ma, L., Li, W. S., Yu, Z. H. *et al.* Epitaxial growth of wafer-scale molybdenum disulfide semiconductor single crystals on sapphire. *Nat Nanotechnol* **16**, 1201-1207 (2021).

27 Ma, K. Y., Zhang, L., Jin, S., Wang, Y., Yoon, S. I. *et al.* Epitaxial single-crystal hexagonal boron nitride multilayers on Ni (111). *Nature* **606**, 88-93 (2022).

28 Wang, L., Xu, X. Z., Zhang, L. N., Qiao, R. X., Wu, M. H. *et al.* Epitaxial growth of a 100-square-centimetre single-crystal hexagonal boron nitride monolayer on copper. *Nature* **570**, 91-95 (2019).

29 Zheng, P. M., Wei, W. Y., Liang, Z. H., Qin, B., Tian, J. P. *et al.* Universal epitaxy of non-centrosymmetric two-dimensional single-crystal metal dichalcogenides. *Nat Commun* **14**, 592 (2023).

30 Komsa, H. P., Kotakoski, J., Kurasch, S., Lehtinen, O., Kaiser, U. *et al.* Two-Dimensional Transition Metal Dichalcogenides under Electron Irradiation: Defect Production and Doping. *Phys Rev Lett* **109**, 035503 (2012).

31 Komsa, H. P., Kurasch, S., Lehtinen, O., Kaiser, U. & Krasheninnikov, A. V. From point to extended defects in two-dimensional MoS_2: Evolution of atomic structure under electron irradiation. *Phys Rev B* **88**, 035301 (2013).

32 Zhou, W., Zou, X. L., Najmaei, S., Liu, Z., Shi, Y. M. *et al.* Intrinsic Structural Defects in Monolayer Molybdenum Disulfide. *Nano Lett* **13**, 2615-2622 (2013).

33 Hong, J. H., Hu, Z. X., Probert, M., Li, K., Lv, D. H. *et al.* Exploring atomic defects in molybdenum disulphide monolayers. *Nat Commun* **6**, 6293 (2015).

34 Mitterreiter, E., Schuler, B., Micevic, A., Hernangómez-Pérez, D., Barthelmi, K. *et al.* The role of chalcogen vacancies for atomic defect emission in MoS_2. *Nat Commun* **12**, 3822 (2021).

Acknowledgements

This work was supported by the National Key R&D Program of China (2022YFA1403503 (X.X.) and 2021YFA1200801(Q.Y.)), the National Natural Science Foundation of China (12322406 (X.X.), 92577101 (X.X.), 52025023 (K.L.), 51991342 (K.L.), 52021006 (K.L.), 22173031 (Q.Y.) and 12474227 (Q.Y.)), Guangdong Major Project of Basic and Applied Basic Research (2021B0301030002 (K.L.)), the Pearl River Talent Recruitment Program of Guangdong Province (2019ZT08C321 (X.X.)), Special Funds for the Cultivation of Guangdong College Students' Scientific and Technological Innovation ("Climbing Program" Special Funds (pdjh2025bk069 (X.X.)), SCNU Training Program of Innovation for Undergraduates (S202510574205 (Z.H.)), the computations were performed at ECNU Multifunctional Platform for Innovation (001).

Author contributions

X.X., K.L. and Q.Y. supervised the project. J.C., Y.Z., Y.C., Q.C., X.L. and Z.H. conducted the sample growth, Q.G. performed the TEM experiments. J.C. performed the optical measurements. J.C. performed the AFM experiments. Y.G. and Q.Y. performed the theoretical calculations. M.L., K.L., Y.Z., B.Z. and Y.H. performed the STM experiments. J.C., Z.L. and Q.Y. performed the electrical experiments. X.X., K.L. and Q.Y. wrote the article. All of the authors discussed the results and comments on the paper.

Competing interests

The authors declare no competing interests.

Figure captions

Fig. 1 | Different growth behaviours of WS_2 on MoS_2/sapphire substrates. a, Schematic diagram of WS_2 islands on MoS_2/c-plane sapphire without steps. **b,** Formation energy of WS_2/MoS_2 shown in **(a)** with different rotation angles. The WS_2/MoS_2 sample has two similar minima ($\theta = 0°$ and $\theta = \pm 60°$). Inset: top view of **(a)**. **c,** Statistical distributions of the orientations of WS_2 islands grown on MoS_2 sample under van der Waals (vdW)-guided epitaxy. **d,** Schematic diagram of WS_2 islands on MoS_2/c-plane sapphire with steps. **e,** Formation energy of WS_2/MoS_2 shown in **(d)** with different rotation angles. Inset: top view of **(d)**. **f,** Statistical distributions of the orientations of WS_2 islands grown on MoS_2 sample under step-guided epitaxy**. g,** Schematic diagram of WS_2 islands on MoS_2 with S vacancy at step edges. **h,** Formation energy of WS_2/MoS_2 shown in **(g)** with different rotation angles. Inset: top view of **(g)**. **i,** Statistical distributions of the orientations of WS_2 islands grown on MoS_2 sample under S vacancy/step-guided epitaxy. Insets of **(c)**, **(f)**, and **(i)**: representative optical images of WS_2/MoS_2 samples. The dashed triangles show the edges of MoS_2 islands.

Fig. 2 | Selective formation of S vacancies near step edges. a, Top and side view of relative stress distributions in a stepped MoS_2 structure. **b,** Schematic diagram of MoS_2 with S vacancies at different positions. **c,** Formation energy of MoS_2 samples with S vacancies shown in **(b)**. Inset: top view of MoS_2 with an S vacancy at position S_5. **d,** The Gibbs free energy for WS_2 grown on MoS_2 at the terrace, on MoS_2 at step edges and on MoS_2 with S vacancies at step edges, respectively. Insets: The corresponding schematic diagrams of WS_2/MoS_2. **e-g,** Differential charge density distribution of WS_2 grown on MoS_2 at the terrace **(e)**, on MoS_2 at step edges **(f)** and on MoS_2 with S vacancies at step edges **(g)**, respectively. The purple and green distributions denote electron accumulation and depletion, respectively.

Fig. 3 | Growth of single-crystal WS_2/MoS_2 films. a, Schematic diagrams of the growth process for single-crystal WS_2/MoS_2 films. Single-crystal MoS_2 films were first synthesized, then the S vacancies at step edges were introduced. Subsequently, aligned WS_2 islands can be obtained on MoS_2 and finally seamless stitched into single-crystal WS_2/MoS_2 films. **b-e,** Optical images of as-grown aligned MoS_2 islands on Al_2O_3 **(b)**, continuous MoS_2 film **(c)**, aligned WS_2 islands on MoS_2 film **(e)** and single-crystal WS_2/MoS_2 film.

Fig. 4 | Characterizations of single-crystal WS_2/MoS_2 films. a-b, Photoluminescence (PL) and Raman spectra of MoS_2 (violet lines), WS_2 (dark yellow lines) and WS_2/MoS_2 samples (orange lines). **c-d,** Line scan mapping of PL and Raman spectra of the WS_2/MoS_2 films over 1 cm. **e,** Atomic-resolved atomic force microscopy (AFM) image of the WS_2/MoS_2 film. **f,** Polarized second-harmonic generation (SHG) pattern of the WS_2/MoS_2 film. **g,** Cross-section transmission electron microscopy (TEM) image of the WS_2/MoS_2 film, revealing the rhombohedral-stacked structure. **h,** The local piezoelectric force microscope (PFM) amplitude (orange line) and phase (dark blue line) loops during the switching process of the WS_2/MoS_2 film.

Editorial Summary

Rhombohedral-stacked structures formed by 2D semiconductors are characterized by emerging physical properties, but their bottom-up growth remains challenging. Here, the authors report a chemical vapour deposition method to grow cm-scale rhombohedral-stacked WS_2/MoS_2 crystals with ferroelectric properties.

Peer review information: *Nature Communications* thanks Taesung Kim, Junhao Lin, and the other, anonymous, reviewers for their contribution to the peer review of this work. A peer review file is available.

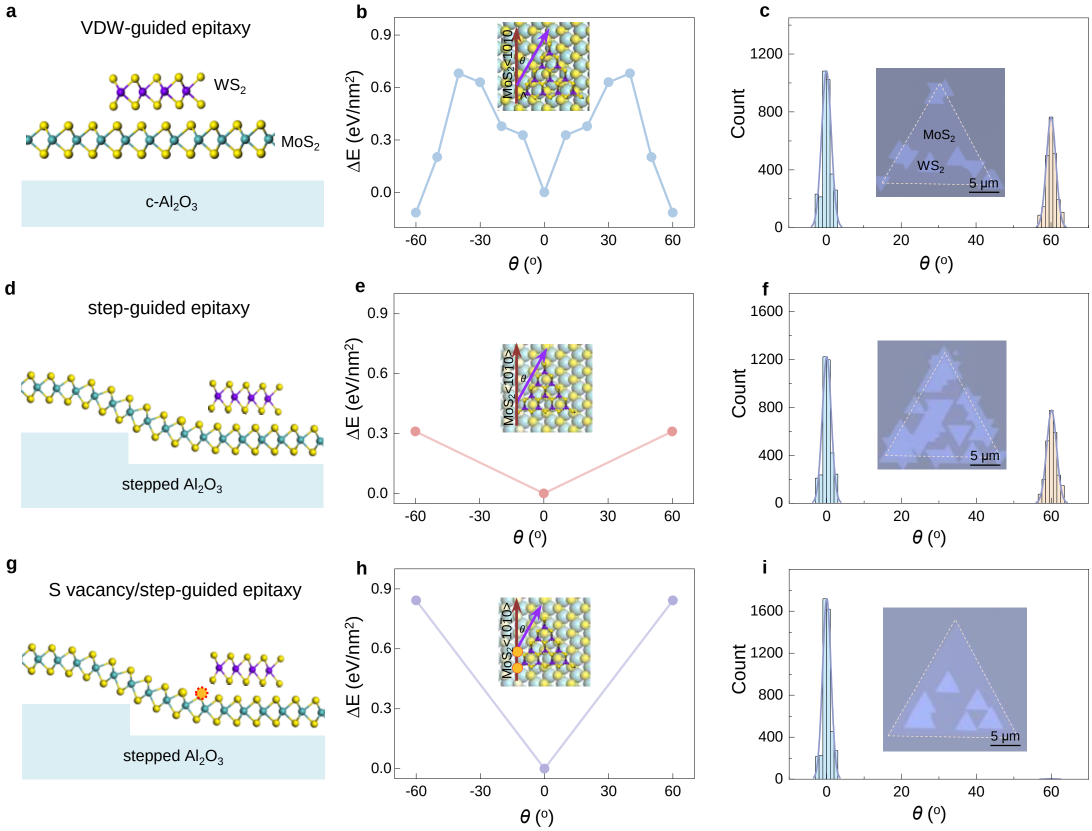
a
VDW-guided epitaxy
WS$_2$
MoS$_2$
c-Al$_2$O$_3$
b
ΔE (eV/nm^2)
0.9
0.6
0.3
0.0
-60
-30
0
30
60
θ (°)
MoS$_2$<10$\bar{1}$0>
θ
c
Count
1200
800
400
0
0
20
40
60
θ (°)
MoS$_2$
WS$_2$
5 μm
d
step-guided epitaxy
stepped Al$_2$O$_3$
e
ΔE (eV/nm^2)
0.9
0.6
0.3
0.0
-60
-30
0
30
60
θ (°)
MoS$_2$<10$\bar{1}$0>
θ
f
Count
1600
1200
800
400
0
0
20
40
60
θ (°)
5 μm
g
S vacancy/step-guided epitaxy
stepped Al$_2$O$_3$
h
ΔE (eV/nm^2)
0.9
0.6
0.3
0.0
-60
-30
0
30
60
θ (°)
MoS$_2$<10$\bar{1}$0>
θ
i
Count
1600
1200
800
400
0
0
20
40
60
θ (°)
5 μm

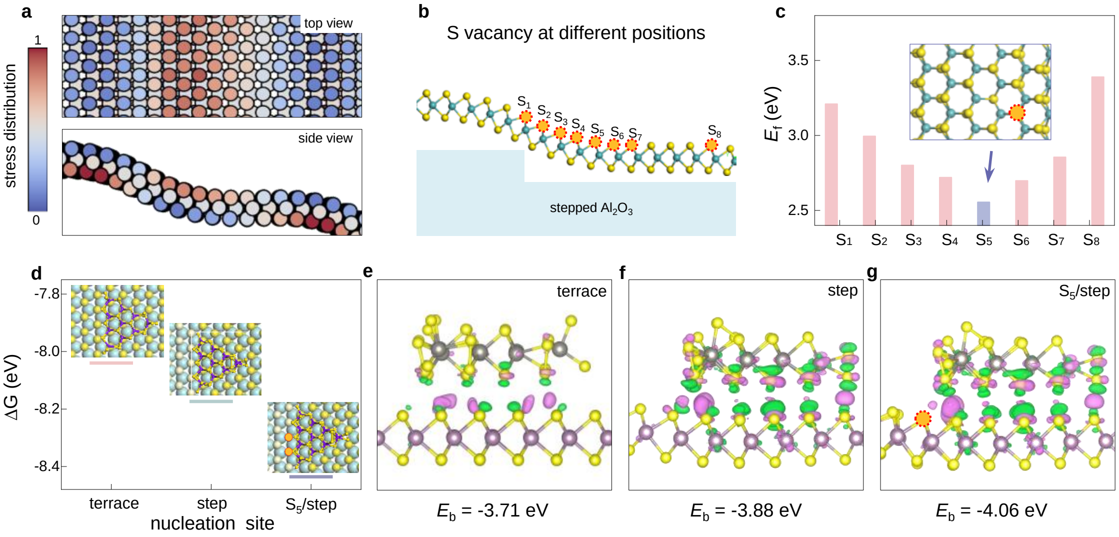
a
top view
side view
stress distribution
1
0
b
S vacancy at different positions
S_1 S_2 S_3 S_4 S_5 S_6 S_7 S_8
stepped Al_2O_3
c
E_f (eV)
3.5
3.0
2.5
S1 S2 S3 S4 S5 S6 S7 S8
d
ΔG (eV)
-7.8
-8.0
-8.2
-8.4
terrace
step
S_5/step
nucleation site
e
terrace
E_b = -3.71 eV
f
step
E_b = -3.88 eV
g
S_5/step
E_b = -4.06 eV

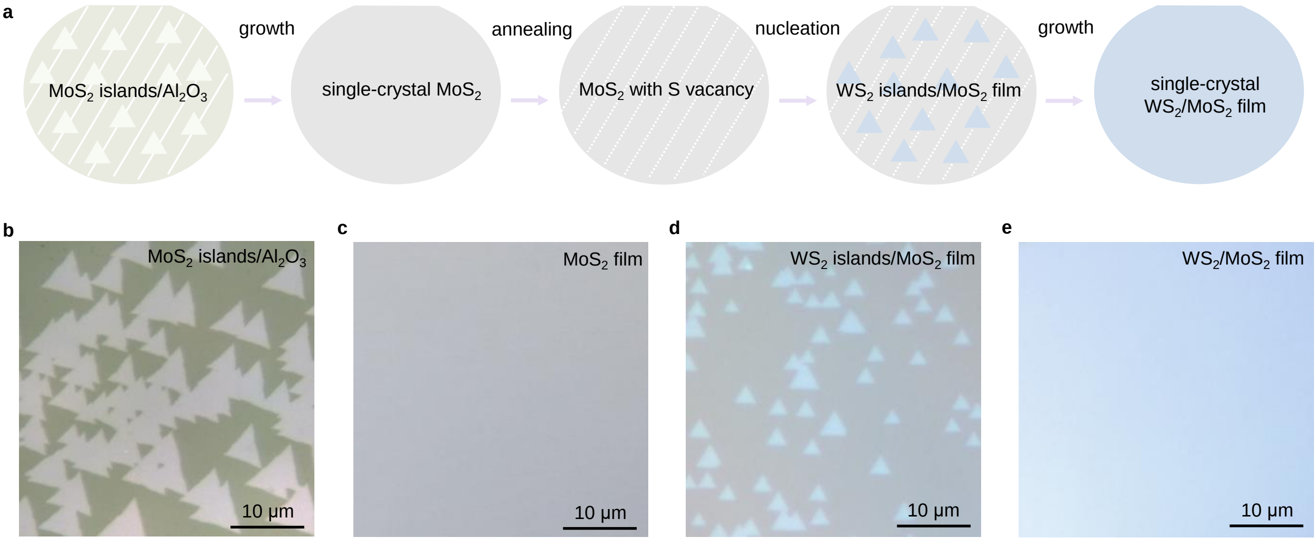
a
MoS2 islands/Al2O3
growth
single-crystal MoS2
annealing
MoS2 with S vacancy
nucleation
WS2 islands/MoS2 film
growth
single-crystal WS2/MoS2 film
b
MoS2 islands/Al2O3
10 μm
c
MoS2 film
10 μm
d
WS2 islands/MoS2 film
10 μm
e
WS2/MoS2 film
10 μm

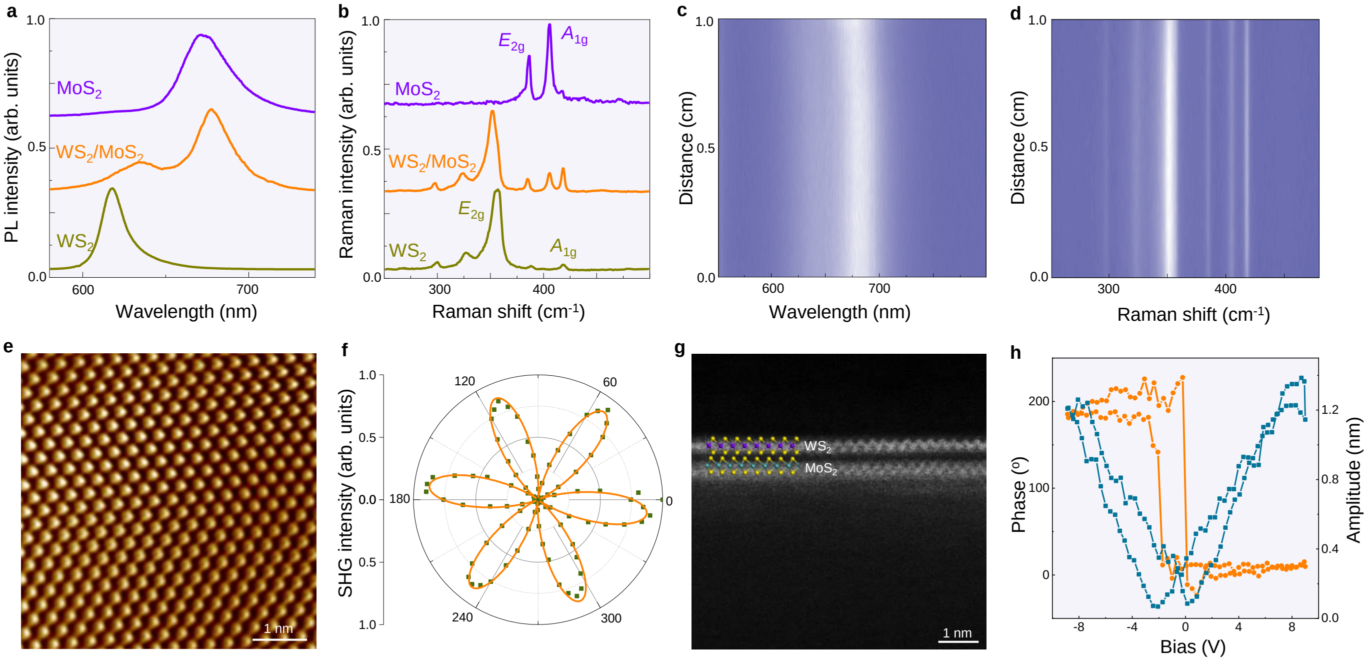
a
1.0
0.5
0.0
PL intensity (arb. units)
MoS$_2$
WS$_2$/MoS$_2$
WS$_2$
600
700
Wavelength (nm)
b
1.0
0.5
0.0
Raman intensity (arb. units)
E_{2g}
A_{1g}
MoS$_2$
WS$_2$/MoS$_2$
E_{2g}
WS$_2$
A_{1g}
300
400
Raman shift (cm^{-1})
c
1.0
0.5
0.0
Distance (cm)
600
700
Wavelength (nm)
d
1.0
0.5
0.0
Distance (cm)
300
400
Raman shift (cm^{-1})
e
1 nm
f
1.0
0.5
0.0
0.5
1.0
SHG intensity (arb. units)
120
60
180
0
240
300
g
WS$_2$
MoS$_2$
1 nm
h
200
100
0
Phase (°)
1.2
0.8
0.4
0.0
Amplitude (nm)
-8
-4
0
4
8
Bias (V)